ELSEVIER

Chemical Engineering Journal 68 (1997) 197–205

Chemical Engineering Journal

Simulation of the performance of electrical capacitance tomography for measurement of dense phase pneumatic conveying [1]

K.L. Ostrowski *, S.P. Luke, R.A. Williams

Virtual Centre for Industrial Process Tomography, Particle and Colloid Engineering Group, Camborne School of Mines, University of Exeter, Redruth, Cornwall TR15 3SE, UK

Received 3 February 1997; revised 25 July 1997; accepted 8 August 1997

Abstract

A method for the estimation of image distortion which can occur in the reconstruction of electrical capacitance tomography (ECT) data for pneumatic conveying process is presented. Image distortion is associated the finite sampling rate of tomographic instrumentation which arises from changes in the distribution of phases occurring during a measurement cycle. The method uses an algorithm which provides the solution of the *inverse* and *forward problems* for an idealized 2-D sensor and to visualize the movement of powder slugs. The influence of the geometry of the sensor electrodes and the nature of slug perturbation on the fidelity of the reconstructed image is discussed. The practical implications of the simulation for the application of capacitance tomography for monitoring and control of dense phase conveying are discussed. © 1997 Elsevier Science S.A.

Keywords: Image distortion; Powder slugs; Slug perturbation; Capacitance tomography

1. Introduction

Electrical capacitance tomography (ECT) is gaining acceptance as a laboratory and on-line tool to analyze multiphase systems such as powder conveying [1], powder fluidisation [2–4] and oil/water/gas transport [5,6]. Some of the first reported industrial trials in which sensor arrays were installed in pneumatic conveying systems considered lean phase [1,3] and dense phase [2] systems. For lean phase conveying the imaging method enabled important fault conditions (such as the development of saltation layers at the bottom of the pipe cross-section) to be observed and hence decisions could be made on the degree of suspension of the solid particulates. The sensitivity of the method did not allow concentration gradients within the pipe to be perceived since, for the material used, detectable differences in the dielectric constant did not occur until the volume fraction of solid exceeded about 0.07. In dense phase conveying the arrival of powder slugs could be observed and the wave velocity of this perturbation could be estimated, but in using only an 8-electrode system [1,6] the images were crude and subject to noise such that details of the slug geometry could not be elucidated. There remains therefore a need for designers of pneumatic conveying systems to have a reliable means of observing the nature of the flow of powders in dense phase conveying so that optimum plant design and operation conditions can be achieved [7,8]. In particular, information on the size, shape, length and frequency of slugs moving in conveyors is sought. This provides the primary focus for the present paper, in which we consider the feasibility of using single and multiple capacitance sensor arrays each containing 12-capacitance electrodes. A key question is to see if the passage of slugs can be visualized accurately and, in the longer term, to compute details concerning the shape of the front and rear edges of the slugs.

An ECT system has three basic units (Fig. 1): the sensor, the electronics control panel and the host computer supported by the set of transputers as described in detail elsewhere [9]. The sensor consists of a number of sensing and guard electrodes usually placed outside or embedded within an insulating pipe. The resolution of reconstructed images and speed of frame capture strongly depend on the number of electrodes. The electronic system provides fast and accurate measurement of the capacitance for all possible electrodes connections. The host computer controls the measurement process and parameters and also formulates the captured data to obtain the reconstructed image using an appropriate algorithm [10].

* Corresponding author.

[1] Dedicated to the memory of David Leyland whose sudden death was a great loss to the capacitance tomography research team.

PII S1385-8947(97)00095-8

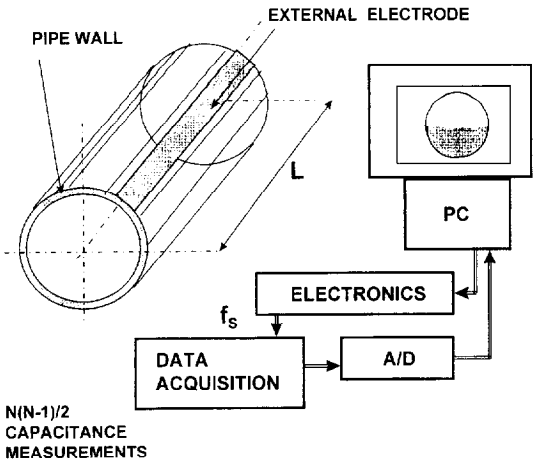

Fig. 1. Principles of capacitance imaging.

For a typical system with only one source electrode the number of measurements obtained (i.e., the number of pieces of information on the electrostatic field and its related dielectric constant distribution in the sensing region) is equal to $N(N-1)/2$ where N is the number of electrodes. The reconstructed image resolution is approximately proportional to the number of independent inter-electrode measurements, while the speed of frame capture is inversely proportional to the number of such measurements. Thus, contrary to the philosophy of medical tomography in which many 'views' are obtained to provide a high resolution image, the ECT system designed for pneumatic conveying control and monitoring has a relatively low number of electrodes ($N=6$, 8 or 12). For example, a recent commercially available ECT system with a 12 electrode sensor provides a data capture rate equal to about 100 frames s^{-1} and resolution equal to ca. 5% (i.e., the size of the target object to be visualized should be at least 5% of pipe diameter) assuming there is large enough difference of dielectric constant between the powder slug and the surrounding medium. [2] Yang et al. [6] have discussed the critical features associated with the design of the hardware within an ECT system including: the type of the measuring circuit; the need for high measurement resolution (ca. 0.3 fF); low noise level (rms < 0.1 fF); low baseline drift but a wide dynamic range of measurement (from 0.3 fF up to 2000 fF).

In the present paper we consider the practical consequences of using a state of the art ECT system to monitor the behavior of a dense phase powder conveying system. The issue of the image reconstruction errors resulting from the finite velocity of a fast-moving solid slug passing through the sensor is considered.

Such slugs were observed by the authors in a pilot-scale vacuum conveying system, which motivated the development of present analysis. The system has been designed as a closed loop for solids and an as open system for air. Solids (nylon plastic pellets having bulk density = 750 kg m^{-3}, solid density = 1120 kg m^{-3} and size = 2–4 mm) sucked from a storage hopper are transferred through an standpipe 11 m in length and stored in the vacuum conveyor. Induced air is pushed through a filter and removed by a vacuum pump to atmosphere. Vacuum is achieved using a multistage injector driven by air supplied from compressor. Using this arrangement the maximum induced air and solid flow rates were 1.2 10^{-3} Nm^3 s^{-1} and 18 kg h^{-1}, respectively. This range of flow rates was sufficient to generate a wide range of flow patterns, from dense slug flow up to dilute, fast flow at low solid concentration.

In order to facilitate visual observations of the flow regime the 3 m horizontal test section in the conveyor was fabricated from transparent pipe. Thus by combining the ECT data with images provided by a video camera estimates of slug length and velocity could be obtained. Table 1 presents a set of typical values of slug characteristics for four different operating conditions corresponding to different air flow rates. Note that slug velocities can exceed 2.5 ms^{-1}. Fig. 2 shows a measured 3-D visualization of a powder slug passing through the ECT sensor.

[2] M. Byars, Process Tomography, Cheshire, personal communication, 1996.

Table 1
Typical mean length and velocity of powder slugs for different conditions obtained in a pilot-plant dense-phase pneumatic conveying

Operating conditions	Slug length λ_S [m]	Mean slug velocity c [ms^{-1}]	Air flow rate [$Nm^3 s^{-1}$] × 10^3	Solid flow rate [kg h^{-1}]
A	0.9	0.8	0.89	15.2
B	0.8	1.5	0.48	13.4
C	0.8	2.5	0.79	15.1
D	0.7	2.9	0.93	16.4

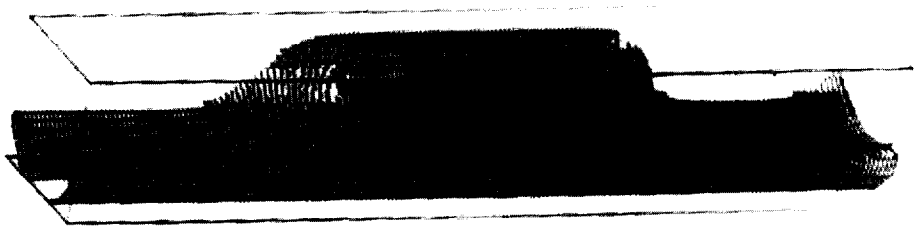

Fig. 2. Image of powder slug ca. 0.8 m long passing through ECT sensor with velocity equal to about 2.5 m/s.

2. Principle of image reconstruction

Image reconstruction algorithms used in ECT can be divided into three main groups based on methods involving linear back-projection (LBP) [10,11], iterative solutions and neutral networks [12]. The LBP algorithm is qualitative and can yield low quality images. However, since it is the simplest and the fastest, which is essential in the monitoring of fast perturbations it was the method chosen for the present practical analysis.

According to LBP approach the response of the sensor (change of capacitance of each electrodes pair) may be found as superposition (linear model) of interaction which result when the dielectric constant of one small element – a pixel placed in the sensing region is changed. Linearity means that these changes are small (interactions between pixels are neglected) so the amount of each change has no influence on method of calculation (however, it does influence signal resolution). In practice it is convenient to replace the dielectric constant ε by its normalized value $\varepsilon_N (0 < \varepsilon_N < 1)$:

$$\varepsilon_N = \frac{\varepsilon - \varepsilon_{MIN}}{\varepsilon_{MAX} - \varepsilon_{MIN}}, \tag{1}$$

similarly, the analogous definition may be introduced for normalized capacitance:

$$C_N = \frac{C - C_{MIN}}{C_{MAX} - C_{MIN}} \tag{2}$$

where minimum and maximum values of capacitance correspond with the situations when sensor is filled with a medium having minimum or maximum dielectric constant.

The LBP algorithm is based on obtaining, a priori, the capacitance sensitivity distribution for all possible single-electrode combinations and all pixels. The distribution of sensitivity – *sensitivity map* depends on the method of its calculation, the shape and size of the pixels and arrangement of the pixels in the cross-section. For the software used here, the image screen contains 1024 square pixels based on 32×32 Cartesian mesh (Fig. 3). The total number of pixels placed into sensing region is 820. Note that size of pixel is 3.15% of the sensor ID, which for 12 electrode sensor gives ca. half of the resolution. Now for connection between electrodes n, m the normalized capacitance may be expressed as linear combination for all pixels i, j, where i and j are the number of columns and rows, respectively:

$$C_{N\,n,m} = \sum_{i=1,32;\ j=1,32} s_{n,m}(i,j)\,\varepsilon(i,j) \tag{3}$$

where $s_{n,m}(i,j)$ is the sensitivity of i,j pixel for n,m electrodes combination, assuming that the sensitivity is equal to zero for all pixels placed outside the sensing region. Eq. (3) may be interpreted as nondimensional solution of the LBP *forward problem* from which is seen that:

$$1 = \sum_{i=1,32;\ j=1,32} s_{n,m}(i,j) \tag{4}$$

The solution of the LBP *inverse problem* may be written as:

$$\varepsilon_N(i,j) = \sum_{N=1}^{N-1} \sum_{m=n+1}^{N} C_{N\,n,m} s_{n,m}(i,j) g_{n,m} / \left\{ \sum_{n=1}^{N-1} \sum_{m=n+1}^{N} s_{n,m}(i,j) g_{n,m} \right\} \tag{5}$$

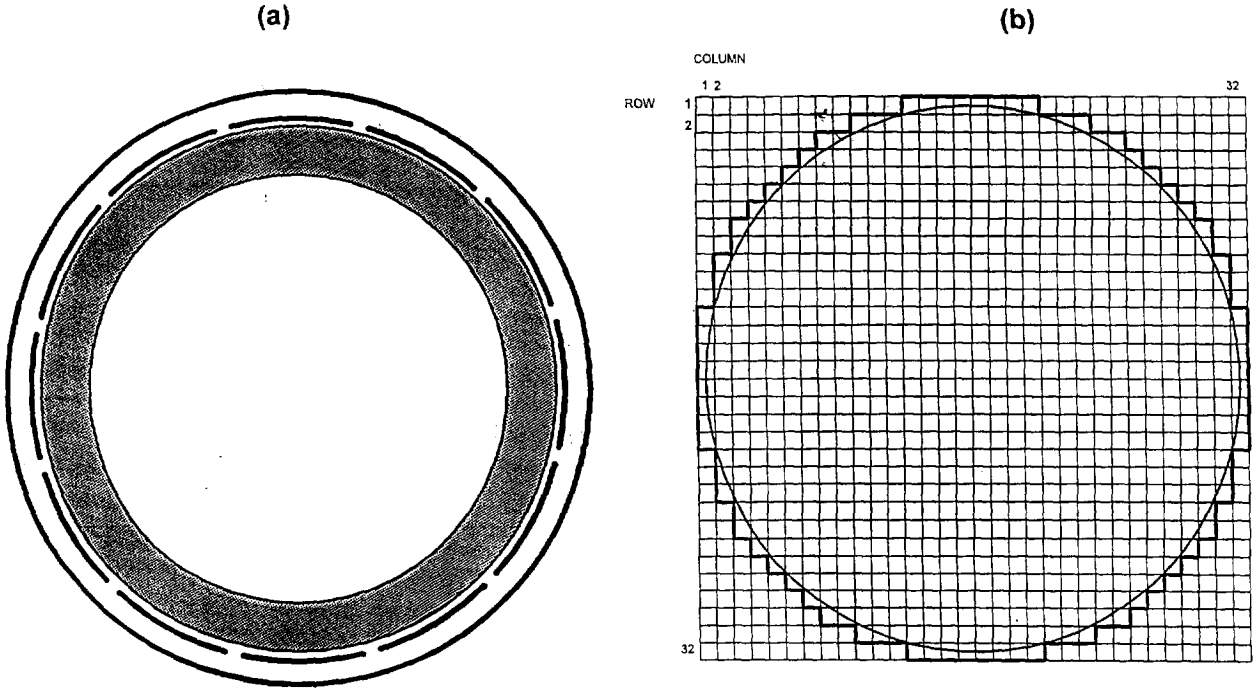

Fig. 3. (a) Cross section of ECT sensor; (b) Cartesian mesh used in present analysis.

where $g_{n,m}$ are the *weighting coefficient* defined for a given sensitivity map and resulting from different C increments for the same increments of ε. Their values depends also on the type of the mesh and method of calculation, e.g., the coefficient for the pair 1–2 differs from this for pair 2–3 because of different pixels arrangement. This difference may vanish for the mesh based on the polar coordinates, however for the mesh presented in Fig. 3 the reconstructed image may depend on the position of electrode no. 1. For the algorithm used here this electrode is placed to the right from the sensor centre, i.e., between clock positions 2.30 and 3.30. The other eleven electrodes are equal-spaced in anti-clock wise direction.

3. Problem formulation and method of solution

The values of sensitivity relating to a particular pixel strongly depends on its position with respect to the source (excitation) and detecting electrodes. Absolute values of sensitivity are large in the vicinities of these electrodes and relatively small in the rest of the sensing region. For the 12 electrode sensor, data capture starts when electrode no. 1 is a source electrode and electrodes from 2 up to 12 are detecting. Then electrode no.2 becomes a source and correspondingly electrodes from 3 up to 12 are detecting. The last measurement is completed when electrodes no. 11 and 12 are source and detecting electrodes, respectively.

Because of this order of field excitations the sensitivities of particular regions inside the sensor change in time. Generally, when the process starts the most sensitive are those which lie placed close to the electrodes having low numbers and on completion of the cycle it correspond to regions close to the high numbered electrodes. If the physical phenomena to be observed are slow enough this effect does not matter. However, when the perturbation being monitored is fast the order in which data is captured may deform the shape of reconstructed slug. The present contribution seeks to identify circumstance where caution must be exercised.

For example, for electrode sensors which are 0.1 m in length ($L=0.1$ m, Fig. 1) during 0.01 s (a typical time required for frame capture for the 12 electrodes sensor) a powder slug moving with velocity of 1 m/s will occupy 10% of sensor length. This value will increase up to 30% for a sensor of minimum practical length of around 0.03 m. Since the current trend in sensor design is to decrease the length of sensing regions this phenomenon will tend to become increasingly important in determining the quality of reconstructed images.

For the sake of simplicity we will consider the special form of perturbation which consist of two regions (Figs. 4 and 5):

bottom region filled with solid bed of constant dielectric constant ($\varepsilon_N=1$),
upper region filled with gas of constant dielectric constant ($\varepsilon_N=0$).

The perturbation of this type is fully determined by gas/solid interface shape and its movement and there are basic assumptions we shall adopt regarding this perturbation.

The perturbation is nondispersive and its velocity is constant, i.e., frequency, wave number and velocity obey the relation:

$$\frac{\omega}{k}=\frac{\mathrm{d}\omega}{\mathrm{d}k}=c=\text{constant}. \tag{6}$$

The perturbation is two-dimensional, i.e., altitude of gas/solid interface is constant for the given cross-section (Fig. 4).

The gas/solid interface is modelled as a 'quasi-step' function (Fig. 5) and determined by the following parameters:

maximum and minimum solid level (A_{max}, A_{min}),
wavelength of perturbation ($\lambda=2\pi/k$),
front-length, slug-length and tail-length (λ_F, λ_S, λ_T).

It is also assumed that all 3-D phenomena may be neglected including the displacement of the electrostatic field not only in the vicinity of the inlet and outlet sections but also in the centre of the sensing region as a result of nonzero inclination of the gas/solid interface (Fig. 6).

According to the 2-D approach the sensitivity distribution is the same for all sensors cross-sections so that the value of ε_N for given pixel may be interpreted as the averaged value, integrated along sensor axial length – L (Fig. 4).

An algorithm was prepared in order to estimate the reconstruction effects based on Eqs. (3)–(5), as summarized in Fig. 7. The algorithm consists of three parts. In the first, the initial set of data is input. The second part calculates the distribution of real value of normalized dielectric constant by integration for each pixel along the sensor length at the

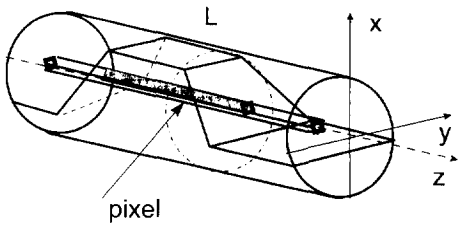

Fig. 4. 2-D powder slug passing through the sensor and single pixel filled partially with solid and partially with gas.

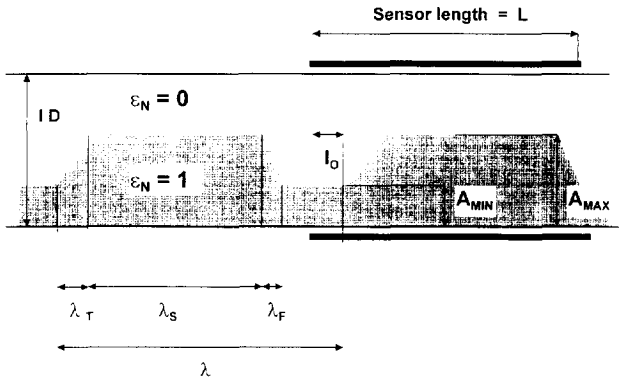

Fig. 5. The form of powder slug considered in this paper.

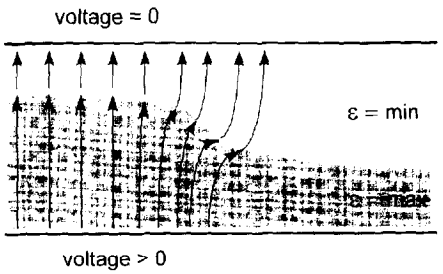

Fig. 6. Schematic illustration of electrostatic field displacement resulting from 3-D effects neglected in present model.

moment of measurement. Then the value of normalized n, m electrodes combination capacitance may be calculated using Eq. (3). When this step is repeated $(N-1)N/2$ times then measurements for one image are completed, i.e., *forward problem* is solved. Also the averaged distribution of ε_N – in time and along z-axis – is calculated providing the 'real' image.

The final block of the algorithm solves the *inverse problem* by means of Eq. (5) and repeating the calculation of reconstructed value of dielectric constant $i \times j$ times. At this moment the simulation of the capture of one frame is completed and some additional parameters may be calculated,

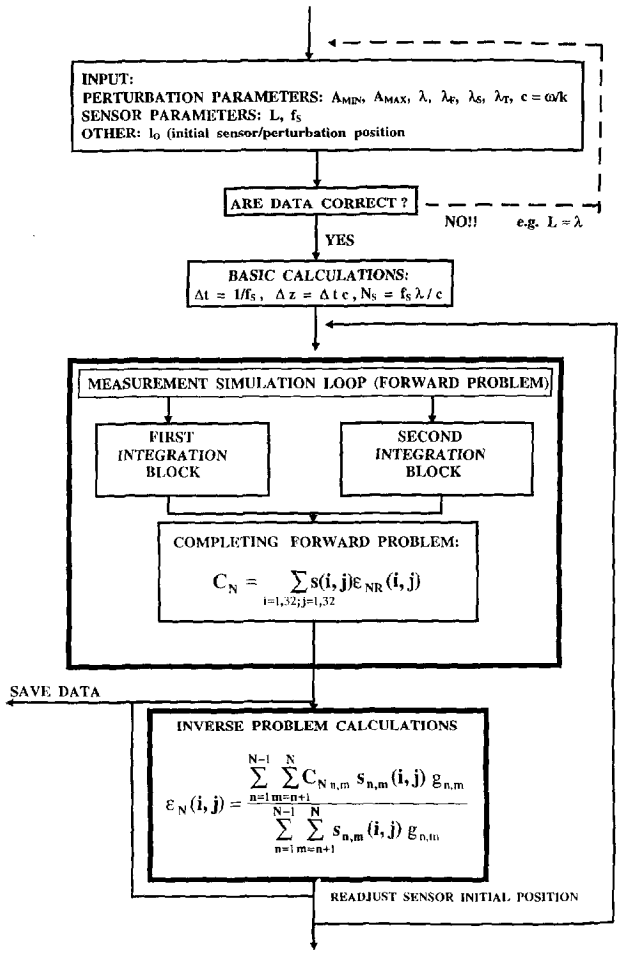

Fig. 7. Flow chart summarising the algorithm simulating measurement of capacitance and solving the inverse problem.

e.g., the time and volume-averaged solid volume fraction in the sensing region. The calculation procedure process is then repeated many times providing the required number of frames to be captured. The results can be visualized frame-by-frame or in the form of an animation of the slugs flowing.

4. Results

Even for the simplified form of perturbation considered above, the number of independent variables is equal to ten. Thus it is difficult to present the clear and comprehensive analysis of influence of particular parameters on image distortion. The definition of 'image distortion' may be formulated in several ways and is of necessity somewhat arbitrary. In this situation it seems reasonable to consider the perturbation of a known shape and known initial position. In such an approach the errors resulting from finite sampling frequency are determined by only two nondimensional groups which may be chosen. We suggest two such grouping which have a simple physical kinematic interpretation:

$$G_1 = \frac{(N-1)N}{2}\frac{c}{f_S L}, \tag{6a}$$

and

$$G_2 = L/\lambda. \tag{7}$$

G_1 may be interpreted as the ratio of perturbation displacement during one frame capture to the length of the sensor. When $G_1 \to 0$ no absolute errors (i.e., the differences between the real and reconstructed values of normalized dielectric constant) resulting from finite sampling rate f_S should occur. If $G_1 < 1$, then any change of its value causes significant distortion of reconstructed image since the changes of solid volume fraction become larger. For $G_1 > 1$ the response of the system strongly depends on the perturbation parameters and no generalized prediction is possible. In a special case, as the slug length tends to infinity the errors in reconstructed image also tends to zero when $G_1 \to \infty$. However, this dependence does not have to be monotonical. Contrary to G_1, incrementing G_2 decreases the relative errors in image reconstruction because as the sensor length L increases the relative changes of solid volume fraction are smaller. However, interpretation of G_2 is not so simple as of G_1. For example when G_2 tends to a whole number, the sensor becomes insensitive and the image reconstruction errors cannot be correctly defined.

Selected examples of comparison between the real and reconstructed images are presented in Figs. 8–12. Fig. 8 shows a 'no perturbation' case corresponding to a static image with the bottom part of sensor filled with solids and the upper region with gas. Thus $G_1 = 0$ and errors of reconstructed image result only from inverse problem solution, but not from finite sampling frequency itself. Note, that in Fig. 8, as well as in Figs. 9–12, the range of reconstructed values of nor-

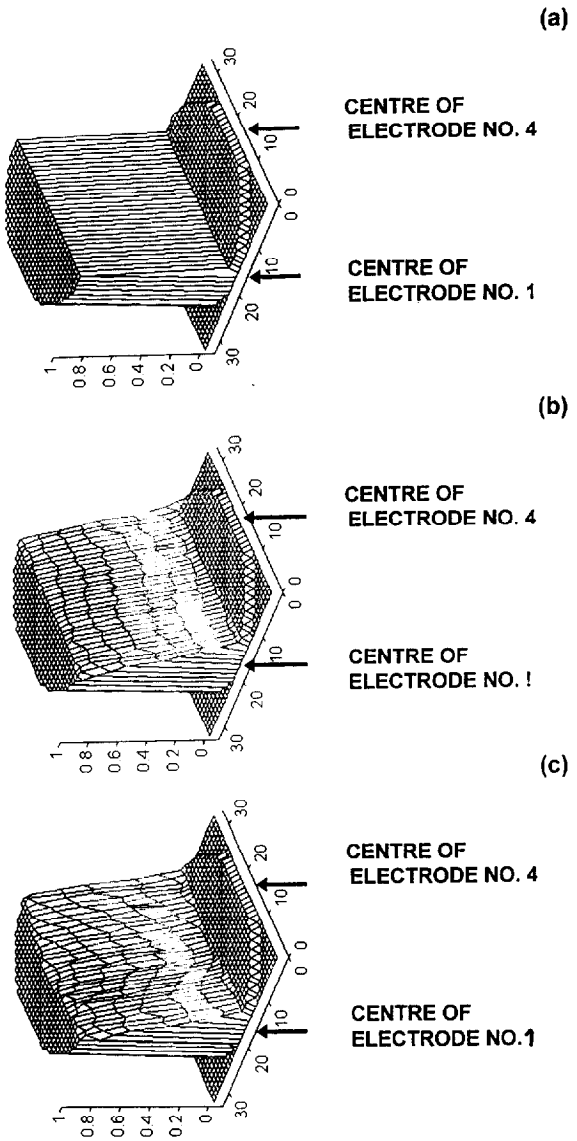

Fig. 8. (a) Actual (resulting from input perturbation); (b) Calculated in present analysis; (c) Reconstructed by ECT measuring system images for bottom part of sensor filled with solid and upper with gas. All pixels placed outside the sensing region have attributed value of −0.05 to make its boundary more clear.

malized dielectric constant is limited to 0 to 1 which provides a constant resolution for the depicted distributions.

Figs. 9–12 illustrate the image distortion for $G_2=0.1$ and $G_1=0.33$, 0.66, 1.66, 3.33, which for example when $(N-1)N/2f_S=0.01$ s and $L=0.03$ m corresponds with the perturbation velocities: 1, 2, 5 and 10 m/s, respectively. The shapes of slugs are determined as follows:

$A_{MIN}=0.25ID$, $A_{MAX}=0.75ID$, $\lambda_F/\lambda=0.1$ $\lambda_S/\lambda=0.5$,

$A_{MIN}=0.25ID$, $A_{MAX}=0.75ID$, $\lambda_F/\lambda=0$ $\lambda_S/\lambda=0.5$,

$A_{MIN}=0$, $A_{MAX}=ID$, $\lambda_F/\lambda=0$ $\lambda_S/\lambda=0.5$.

Generally, the distortion of the image is manifested as 'undershooting' appearing in the vicinity of the 'low number' electrodes and 'overshooting' typical for regions placed near

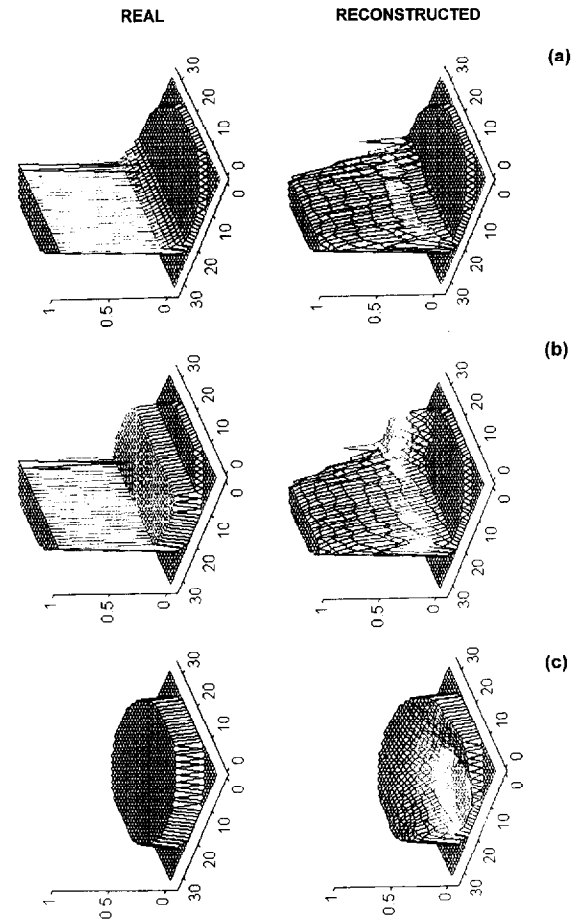

Fig. 9. Real (left) and reconstructed (right) images obtained for $G_1=0.33$, $G_2=0.1$, $l_0=0$, and: (a) $A_{MIN}=0.25ID$, $A_{MAX}=0.75ID$, $\lambda_F/\lambda=0.1$, $\lambda_S/\lambda=0.5$; (b) $A_{MIN}=0.25ID$, $A_{MAX}=0.75ID$, $\lambda_F/\lambda=0$ $\lambda_S/\lambda=0.5$; (c) $A_{MIN}=0$, $A_{MAX}=ID$, $\lambda_F/\lambda=0$ $\lambda_S/\lambda=0.5$. All pixels placed outside the sensing region have attributed value of −0.05 to make its boundary more clear.

'high numbers' electrode. This is particularly visible in Fig. 12(c) showing the deflection of the image of a discrete slug which moves like a piston through the sensor. It is clear that averaged normalized dielectric constant is equal to zero in the vicinity of the first electrode instead of a real value close to 0.9.

It should be noted out that the slug velocities (celerities) resulting from the given values of G_1 numbers are larger than the observed in practice. Typical reported values obtained for the laboratory scale measurements (e.g., Ref. [1]) do not exceed ca. 0.5 m/s.

For this perturbation velocity the absolute errors of the normalized dielectric constant distribution may be neglected when compared with the total range of 0 to 1. The situation changes when the relative differences between the real and reconstructed increments are taken into account. In the 'sensor zone' (i.e., the region placed between the two layers constantly filled with gas and solid), these differences are large and there is no clear relation between them and G_1 number. However, they may be influenced by the shape of slug (compare the discrete and nondiscrete slugs in Ref.

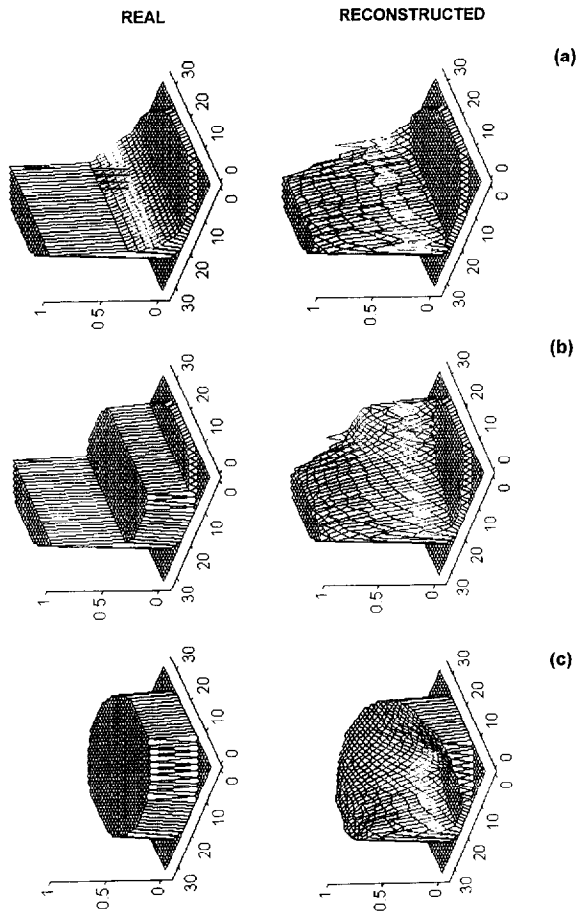

Fig. 10. Real (left) and reconstructed (right) images obtained for $G_1 = 0.66$, $G_2 = 0.1$, $l_0 = 0$, and: (a) $A_{MIN} = 0.25ID$, $A_{MAX} = 0.75ID$, $\lambda_F/\lambda = 0.1$ $\lambda_S/\lambda = 0.5$; (b) $A_{MIN} = 0.25ID$, $A_{MAX} = 0.75ID$, $\lambda_F/\lambda = 0$ $\lambda_S/\lambda = 0.5$; (c) $A_{MIN} = 0$, $A_{MAX} = ID$, $\lambda_F/\lambda = 0$ $\lambda_S/\lambda = 0.5$. All pixels placed outside the sensing region have attributed value of -0.05 to make its boundary more clear.

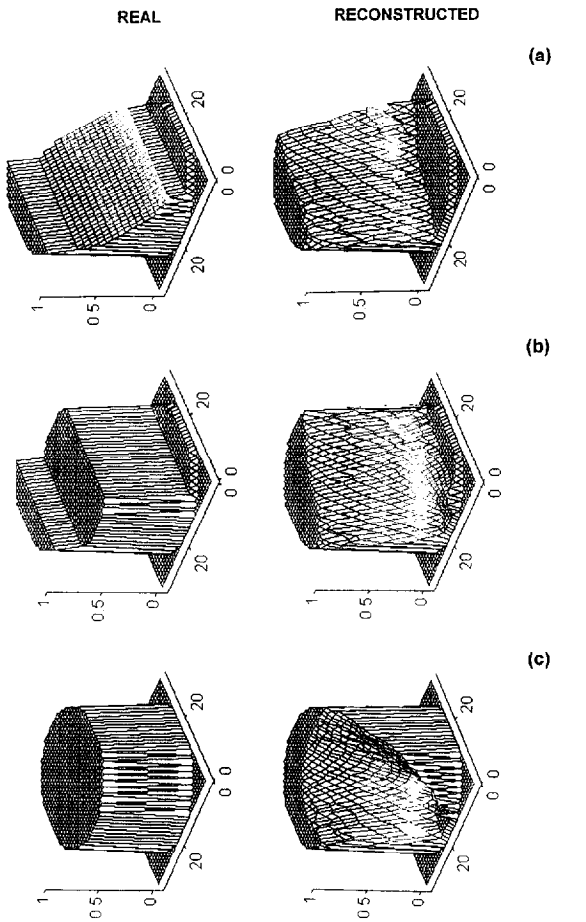

Fig. 11. Real (left) and reconstructed (right) images obtained for $G_1 = 1.65$, $G_2 = 0.1$, $l_0 = 0$, and: (a) $A_{MIN} = 0.25ID$, $A_{MAX} = 0.75ID$, $\lambda_F/\lambda = 0.1$ $\lambda_S/\lambda = 0.5$; (b) $A_{MIN} = 0.25ID$, $A_{MAX} = 0.75ID$, $\lambda_F/\lambda = 0$ $\lambda_S/\lambda = 0.5$; (c) $A_{MIN} = 0$, $A_{MAX} = ID$, $\lambda_F/\lambda = 0$ $\lambda_S/\lambda = 0.5$. All pixels placed outside the sensing region have attributed value of -0.05 to make its boundary more clear.

Figs. 9–12) and by the initial slug position $-l_0$. Thus, G_1 numbers were selected in order to facilitate these observations.

It can be appreciated that regions of undershooting and overshooting present in the same cross-sectional image can effectively cancel out when averaged values over total cross-section are used thus implying low error (Fig. 13) – whereas this may not be true for the particular regions of sensing area. For example in Fig. 13 the relative error of the mean value of ε_N is shown vs. the G_1 number ($G_2 = 0.1$) for two types of perturbations:

$$A_{MIN} = 0,\ A_{MAX} = ID,\ \lambda_F/\lambda = 0\ \lambda_S/\lambda = 0.5$$

and

$$A_{MIN} = 0.5ID,\ A_{MAX} = ID,\ \lambda_F/\lambda = 0\ \lambda_S/\lambda = 0.5.$$

The relative error for *discrete* slug (i.e., for flow regime with no stratified bottom layer) is only about 4% whereas for the case of slug flow with constantly filled bottom part of sensor up to 14%. In the second pattern the overshooting typical for bottom half of sensor cross-section does not appear, which therefore increases the relative error resulting from existing undershooting. From Fig. 13 is clear that errors depends not only on G_1 and G_2 but also on the shape of perturbation and sensing electrodes arrangement.

5. Conclusions

This paper has demonstrated the influence of finite rate of data capture on deflection of reconstructed images. Results were given for a 12 electrode ECT sensor, however they may be extended to other tomography methods based on the LBP algorithm.

Image distortion is influenced by a large number of parameters – thus a comprehensive and general analysis is difficult. In this situation we have concentrated on a simple perturbation simulating slug movement through the sensor in order to estimate effects which may appear in a fast pneumatic conveyor. Two nondimensional numbers have been proposed which provide a trial model of the phenomenon.

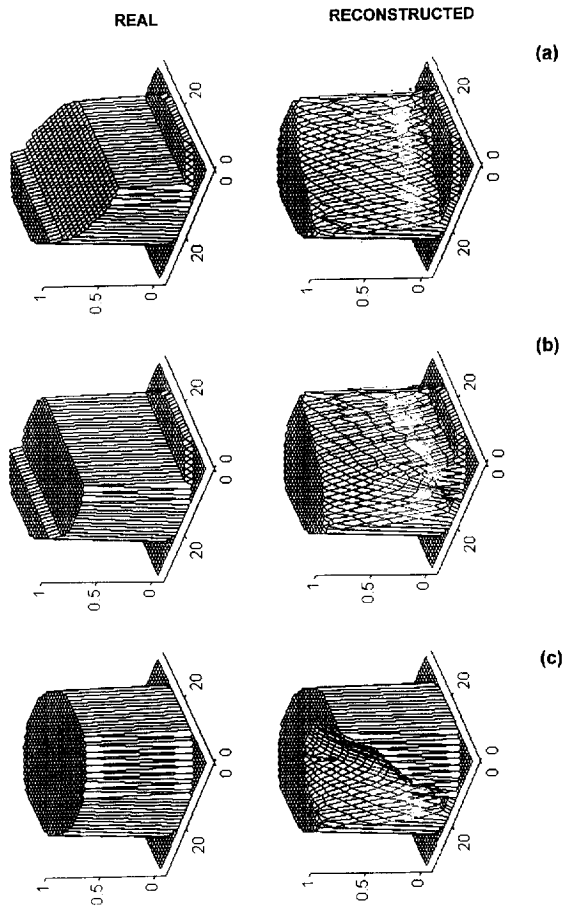

Fig. 12. Real (left) and reconstructed (right) images obtained for $G_1=3.3$, $G_2=0.1$, $l_0=0$, and: (a) $A_{MIN}=0.25ID$, $A_{MAX}=0.75ID$, $\lambda_F/\lambda=0.1$ $\lambda_S/\lambda=0.5$, (b) $A_{MIN}=0.25ID$, $A_{MAX}=0.75ID$, $\lambda_F/\lambda=0$ $\lambda_S/\lambda=0.5$, (c) $A_{MIN}=0$, $A_{MAX}=ID$, $\lambda_F/\lambda=0$ $\lambda_S/\lambda=0.5$. All pixels placed outside the sensing region have attributed value of -0.05 to make its boundary more clear.

The errors associated with a reconstructed image become significant for high velocity slugs or when the rate of data capture is low. The present data capture limitations of existing ECT systems, typically 100 frames s^{-1} for 12 electrode designs, implies that images will suffer significant distortion for high slug velocities exceeding ca. 2 m s^{-1}, when using sensing electrodes of 0.1 m in length. Should the system designer opt for a reduction of the electrode length, typically by the use of driven guard electrodes, the critical value of slug velocity above which distortion occurs is further reduced. These observation apply equally well to other types of nonhomogeneous multiphase flows, e.g., movement of gas slugs in oil.

It is obviously difficult to precisely quantify what effect image distortion would have on the monitoring of dense-phase pneumatic conveyors, but clearly this is largely dependent on the context of the measurement being taken. Under some circumstances, the ramifications for the process engineer are very profound, since as has already been shown, a maximum relative error of close to 15% can be expected for solid volume fraction measurements. This would seem to

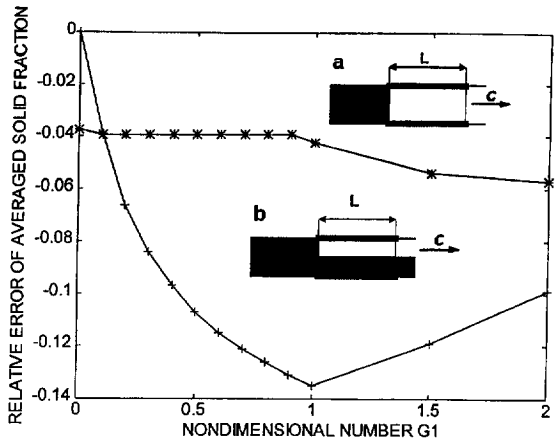

Fig. 13. Relative error of averaged in the sensing volume and data capture time normalised dielectric constant vs. G_1 number for two types of perturbation ($l_0=0$, $\lambda_S/\lambda=0.5$, $G_2=0.1$).

infer that solid flow rate measurements and certainly any control action derived from such measurements can only be reliably achieved from ECT systems when the slug velocity is below the critical value. On the other hand, the effect of image distortion for measurements in other contexts, for example, determination of slug length, perturbation frequency etc., would be far less catastrophic.

The image distortion effect is caused by variations in the activity of electrodes throughout the data capture cycle. For example, electrode no. 1 is only active during the first 17% of the data capture cycle and is subsequently idle. Consequently, the sensor is only sensitive to solid movements within the vicinity of this electrode during the early stages of the measurement process. Fortunately, electrode no. 1 is the worst case example and generally the higher numbered electrodes exhibit a more uniform response in this respect.

Since the contributions of particular electrodes vary in time, their positions around sensing area may influence the final result. This effect will not appear for an *isotropic* flow regime but some patterns observed in pneumatic conveyor are highly *anisotropic*, e.g., *nondiscrete* slug flow with bottom part of pipe filled constantly by solid. In such situation is possible to reduce errors by placing the low numbered electrodes on the bottom part of horizontal pipe, i.e., in the vicinity of regions where steady conditions exist.

The above conclusions provide the first stage of an approach to sensor design for some process tomography applications characterized by relatively high velocity slug which enters or leaves the sensing region. Of course, if the sensor is completely filled with solid during the data capture period (i.e., slug is long enough) no errors resulting from the described effects are observable. Similarly, if the whole perturbation is placed inside sensor (i.e., short slugs) these errors also do not occur. In this case the further tomographic data processing, e.g., auto- and cross-correlation of the signals obtained provides additional information not only on the flow regime but also on the interface velocity distribution.

6. Nomenclature

A_{MAX}, A_{MIN}	maximum and minimum solid level in sensor
c	velocity of perturbation
C	capacitance
C_N	normalized capacitance (Eq. (2))
f_S	frequency of capacitance measurements
G_1	similarity number (Eq. (6))
G_2	similarity number (Eq. (7))
g	weighting coefficient
i, j	column and row numbers of pixel
k	wave number of perturbation
l_0	initial sensor position
L	length of sensing electrode
n, m	numbers of source and detecting electrodes
N	number of electrodes
s	sensitivity
x, y, z	Cartesian coordinates

Greek

ε	dielectric constant
ε_N	normalized dielectric constant (Eq. (1))
λ	wavelength of perturbation
λ_F	length of slug front
λ_S	length of slug
λ_T	length of slug tail
ω	angular frequency of perturbation

Acknowledgements

The authors acknowledge the support of the UK Engineering and Physical Science Research Council through ROPA grant GR/K34757.

References

[1] S.L. McKee, R.A. Williams, T. Dyakowski, T. Bell, T. Allen, Powder Technology 82 (1995) 105–113.

[2] S.J. Wang, T. Dyakowski, C.G. Xie, R.A. Williams, M.S. Beck, Chem. Eng. J. 56 (1995) 95–100.

[3] T. Dyakowski, R.B. Edwards, R.A. Williams, C.G. Xie, Application of capacitance tomography to gas–solid flows, Chem. Eng. Sci. (1997) in press.

[4] J.S. Halow, Capacitance Imaging of Fluidized Bed in Process Tomography: Principles Techniques and Applications, R.A. Williams, M.S. Beck (Eds.), Butterworth-Heinemann, Oxford, 1995, pp. 447–486.

[5] C.G. Xie, N. Reinecke, M.S. Beck, R.A. Williams, Electric Tomography Techniques for Process Engineering Applications, Process Tomography – A Strategy for Industrial Exploitation, M.S. Beck et al. (Eds.), UMIST/ECAPT/EU Brite Euram, Manchester, 1994, pp. 25–32.

[6] W.Q. Yang, M.S. Beck, M. Byars, Meas. Control 28 (1995) 261–266.

[7] S.L. McKee, On-line measurement of particle–fluid transport processes using tomographic techniques, M.S. Thesis, University of Manchester (UMIST), 1992.

[8] G. Klinzing, G. Jama, W. Link, A Study of Plug Breaking in Pneumatic Conveying, Presented at the Pneumatic and Conveying System Conference Sponsored by the Engineering Foundation, Palm Coast, FL, 1996.

[9] R.A. Williams, M.S. Beck (Eds.), Process Tomography – Principles, Techniques and Applications, Butterworth-Heinemann, Oxford, 1995.

[10] C.G. Xie, S.M. Huang, B.S. Hoyle, R. Thorn, C. Lenn, D. Snowden, M.S. Beck, Electrical capacitance tomography for flow imaging: system model for development of image reconstruction algorithms and design of primary sensors, IEE Proc. I, 139, 1992, pp. 89–98.

[11] P.J. Oakley, M.S. Bair, A low cost quantitative reconstruction algorithm for ECT and EIT, in: M.S. Beck et al. (Eds.), Process Tomography – Implementation for Industrial Processes, UMIST/ECAPT/EU, Manchester, 1995, pp. 393–400.

[12] W.Q. Yang, J.C. Gamio, M.S. Beck, An iterative image reconstruction algorithm for electrical capacitance tomography, Meas. Sci. Technol., submitted for publication.